

Quantum confinement and coherent transport in ultrathin Bi2Se3 nanoribbons

Downloaded from: https://research.chalmers.se, 2025-11-20 01:16 UTC

Citation for the original published paper (version of record):

Niherysh, K., Palermo, X., Pullukattuthara Surendran, A. et al (2025). Quantum confinement and coherent transport in ultrathin Bi2Se3 nanoribbons. Scientific Reports, 15(1). http://dx.doi.org/10.1038/s41598-025-23622-7

N.B. When citing this work, cite the original published paper.

research.chalmers.se offers the possibility of retrieving research publications produced at Chalmers University of Technology. It covers all kind of research output: articles, dissertations, conference papers, reports etc. since 2004. research.chalmers.se is administrated and maintained by Chalmers Library

scientific reports



OPEN

Quantum confinement and coherent transport in ultrathin $\mathrm{Bi}_2\mathrm{Se}_3$ nanoribbons

Kiryl Niherysh^{1,2⊠}, Xavier Palermo¹, Ananthu P. Surendran¹, Alexei Kalaboukhov¹, Raitis Sondors¹, Jana Andzane¹, Donats Erts¹, Thilo Bauch¹ & Floriana Lombardi¹

In recent years much progress has been made in realizing topological insulator (TI) nanostructures where the reduced dimensions should help to diminish the contributions from bulk carriers and enhance quantum confinement. Though nm thick 3D-TI nanoribbons exhibiting topological properties are still difficult to reproducibly synthesize. Here we demonstrate the growth of ultrathin ${\bf Bi_2Se_3}$ nanoribbons by a simple catalyst-free physical-vapour deposition, where the tuning of the material evaporation time plays a crucial role in determining the ultimate thickness of the nanoribbons. Magnetotransport and Hall effect measurements show that at thicknesses close to 10 nm the transport features are affected by Altshuler-Aronov-Spivak like coherent orbits at low magnetic fields, while Shubnikov-de Haas oscillations take over at high fields. The observed phenomena originate from the topological surface states and dominate the nanoribbon transport. Ultrathin nanoribbons also show pronounced conductance oscillations as a function of gate voltage, that can be attributed to ballistic transport and quantized sub-bands. The results highlight the importance of material growth to exploit the unique properties of topological surface states, establishing 3D-TI nanoribbons as a promising platform for a variety of novel applications.

Keywords Topological materials, Magnetotransport, Quantum interference effects

The properties of the topologically protected Dirac surface states in 3D topological insulator (3D TI) nanostructures are promising for a variety of applications including quantum computing¹⁻⁴, spintronics⁵⁻⁸, thermoelectric devices⁹⁻¹², and realization of single-electron charge pumps with high accuracy for metrology¹³. However, the contribution from the trivial bulk charge carriers often masks the exotic properties of the topological surface states. To take full advantage of the protected surface states, one needs to tune the chemical potential inside the band gap and close to the Dirac point. One effective way to eliminate the bulk contribution is chemical compensation doping of nanoribbons¹⁴⁻¹⁶; however, this procedure significantly reduces the mobility of surface Dirac electrons^{17,18}. An alternative approach to reduce the bulk contribution maintaining high mobility is to increase the surface-to-volume ratio by growing 3D-TI materials with reduced dimension such as nanoribbons^{19,20}.

In our previous work we demonstrated the growth of ${\bf Bi_2Se_3}$ nanoribbons using our standard catalyst-free physical-vapour deposition (PVD) method²¹. However, in this study, we had a lower yield of nanoribbons with a thickness of less than 15 nm. Here we show that by properly tuning the deposition conditions of our PVD technique, we can identify a regime of growth that allows to obtain stoichiometric ${\bf Bi_2Se_3}$ nanoribbons with thicknesses below 15 nm and lengths up to 5–10 μm . For the thinnest nanoribbons, the growth mechanism changes from a layered to rough regime, varying the morphology of nanostructures, which affects the transport properties of the topological surface states of nanoribbons. In addition to the quantum oscillations in a magnetic field clearly observed in nanoribbons thicker than 15 nm, our combined magnetoresistance and Hall effect measurements reveal a distinct transport regime for thinner ribbons (below 15 nm), where Altshuler-Aronov-Spivak (AAS)-like orbits dominate the transport at low magnetic fields, while Shubnikov-de Haas (SdH) oscillations can still be observed at high fields. Moreover, we demonstrate a clear signature of quantized energy band structure in the form of an oscillatory behaviour of the longitudinal resistance as a function of backgate voltage in our thinnest (12 nm thick) and narrowest (below 100 nm in width) nanoribbons. Overall, our results highlight the importance of material growth and geometrical confinement to be able to use the unique properties of topological surface states for devices beyond the state of the art.

¹Quantum Device Physics Laboratory, Department of Microtechnology and Nanoscience, Chalmers University of Technology, 41296 Göteborg, Sweden. ²Institute of Chemical Physics, Faculty of Science and Technology, University of Latvia, 1586 Riga, Latvia. [⊠]email: niherysh@chalmers.se; floriana.lombardi@chalmers.se

Experimental results and discussion Synthesis of ultrathin ${\bf Bi_2Se_3}$ nanoribbons

 $\mathbf{Bi_2Se_3}$ nanoribbons were synthesized via catalyst-free physical vapour deposition in a GSL-1100X tube furnace (MTI Corporation). $\mathbf{Bi_2Se_3}$ powder was used as a source material, and placed in the center of the furnace tube where the temperature reaches 585 °C during the synthesis. A glass substrate (25×75 mm) was placed downstream from the source material. Before the synthesis, the tube was first flushed with N_2 gas for 5 min to create an inert atmosphere. The scheme of the synthesis process is shown in Fig. 1a.

First, the furnace was heated up from room temperature to 585 °C in a time interval t_1 = 45 min. The substrate temperature at this moment was from 430 to 230 °C at its "hot" and "cold" ends, respectively. After that, the furnace was kept at the temperature of 585 °C for a time t_2 that was varied between 15 (standard growth²¹) and 0 min (modified growth, these work), and afterwards the furnace was turned off to cool down naturally. When the temperature in the furnace center decreased to 540 °C, an N_2 gas flow was introduced in the tube with a dynamic pressure of 26 Torr, initiating the growth of the nanoribbons. The flow was terminated once temperature reached 475 °C, and the tube was filled with N_2 to atmospheric pressure.

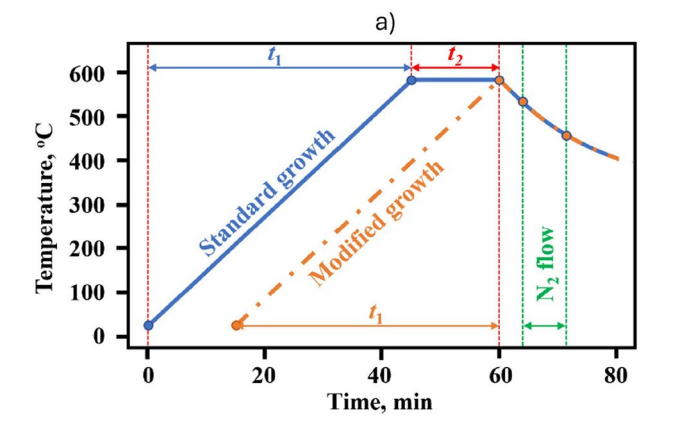
During the standard growth process²¹, nanoplates are deposited on the substrate for a time t_1+t_2 . They serve as seeds for the subsequent formation of nanoribbons during the N_2 streaming. As the top surface of the nanoplate is chemically saturated by selenium atoms²², adatoms adsorbed there from the gas phase cannot form covalent bonds. Thus, they diffuse in the direction of the gas flow and bond to the nanoplate crystal at the edges, which leads to a much faster growth rate in the N_2 flow direction, forming long crystalline nanoribbons²¹. Since the cross-section of the nanoribbons is correlated to that of the seed nanoplates from which they grow, as shown in Fig. 1b, it can be influenced by changing the conditions in which the nanoplates are grown. The amount of deposited material is proportional to the partial pressure of the evaporated source and evaporation time²³, and then the thickness of nanoribbons can be changed by adjusting only these parameters. In this work, the deposition time t_2 was reduced from 15 to 0 min, while the pressures p_1 and p_2 - measured when the heater is switched on and when it reaches the set temperature of 585 °C, respectively - were kept constant.

The synthesis parameters not only influence the geometry of the nanoribbons, but also determine their growth mechanism, affecting their transport properties 24 . Fig. 2a and b show atomic force microscopy (AFM) images and surface profiles for 12 and 22 nm thick nanoribbons, respectively. The thin nanoribbon (Fig. 2a) shows the presence of small grains on the surface, while the thicker one (Fig. 2b) has an atomically flat surface. The average surface roughness for the thin nanoribbon is $\sim 0.67\,$ nm, while for the thicker ribbon this parameter is $\sim 0.13\,$ nm. These images seem to indicate that the growth kinetics of thin nanoribbons differ from that of thick ones.

Here we propose a possible growth scenario that can occur when time t_2 is changed. During the vapour-solid (VS) process, the formation of nanoribbon/nanowire-like nanostructures is determined by growth kinetics^{25,26}. As mentioned earlier, the top surface of the nanoplates (seeds) is chemically saturated. As a result, newly arriving growth species (adatoms) will diffuse to side edges with atomic steps, ledges, and kinks^{27,28}. Previously, it was shown that the two-dimensional nucleation probability on the surface of nanoribbons can be described as^{25–27}:

$$P_N = B \exp\left(-\frac{\pi\sigma^2}{k^2 T^2 \ln\left(p/p_0\right)}\right) \tag{1}$$

where P_N is the nucleation probability, B is a constant, σ is the surface energy, k is the Boltzmann constant, T is the absolute temperature, p is the actual vapour pressure, and p_0 is the equilibrium vapour pressure corresponding to temperature T. If the vapour pressure $p < p_0$, the chemical potential of the crystal is larger than that of the vapour and the crystal should sublimate. However, if $p > p_0$ the vapour should crystallize. In our experiment, the deposition of nanostructures proceeds in the supersaturated state $(p/p_0) > 1$. Therefore,



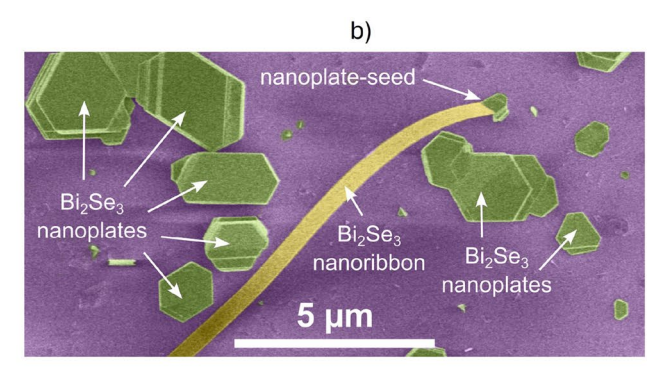


Fig. 1. (a) Schematic of the synthesis process. The solid blue line corresponds to the standard growth described in $Ref.^{21}$, and the orange dot-dashed line corresponds to a modified growth with $t_2 = 0$ min. (b) False-color SEM image of a $\mathbf{Bi_2Se_3}$ nanoribbon and the nanoplate seed.

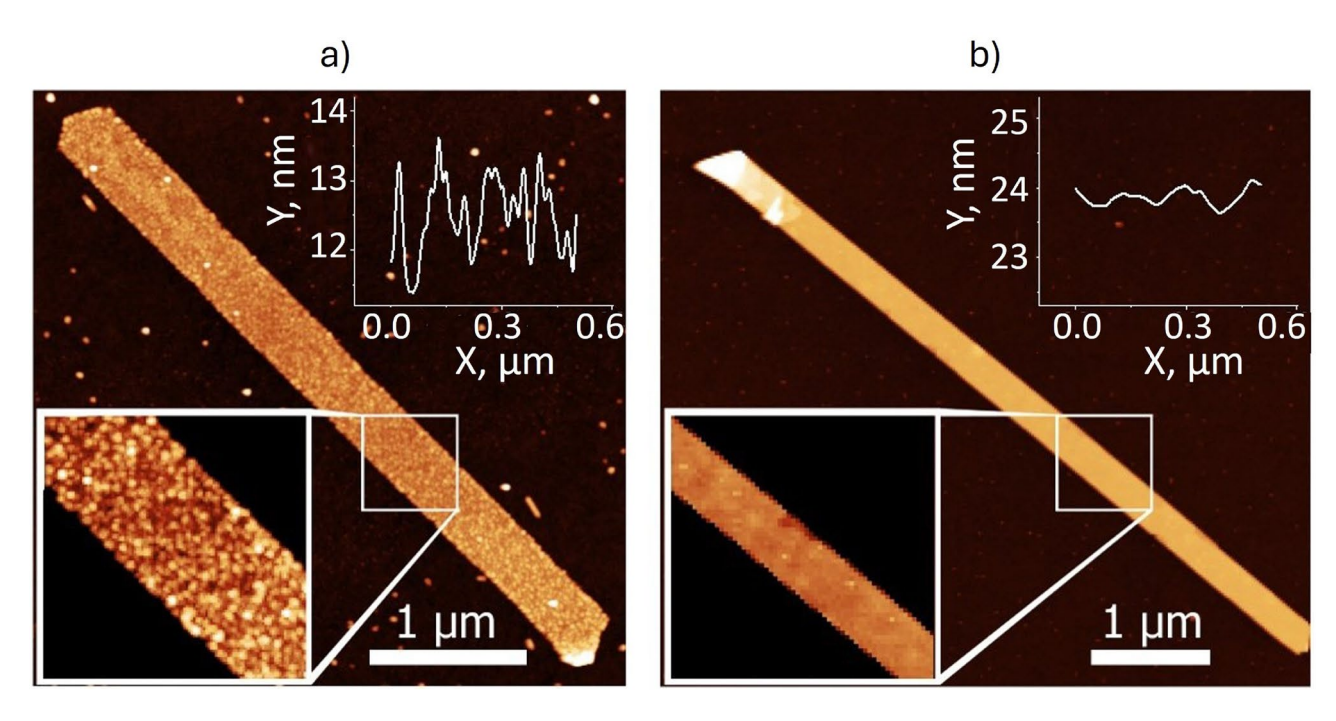


Fig. 2. (a) AFM image of a 12 nm thick nanoribbon grown with the rough mechanism. The inset is the surface profile with RMS roughness around ~ 670 pm. (b) AFM image of a 22 nm thick nanoribbon in which the rough-to-smooth growth transition mechanism occurred. The inset is the surface profile with RMS roughness around ~ 130 pm. The *y*-axis range is identical to the one of the inset in panel (a) to emphasize the significant difference.

the supersaturation ratio (p/p_0) and temperature are two dominant processing factors in controlling the morphology of the products in the VS growth process²⁷.

The amount of evaporated material at the start of nanoribbons growth in the case of $t_2 = 0$ min is much less than in the case of the standard growth, where t₂ = 15 min. Nanoplates (seeds) deposited only over time t₁ have smaller thicknesses in comparison with flakes deposited during time t₁+t₂. However their side edges with atomically rough steps, regardless of the plate thickness, act as effective "catalyst" that initiates the growth of nanoribbons in the lateral direction. As in the case of the vapour-liquid-solid growth mechanism, the edge side area of the "catalyst" plate, from which the nanoribbon growth occurs, can be saturated with adatoms more easily for thinner seeds compared to thicker ones²⁹. The value of supersaturation at the edge surface tends to decrease for plates with higher thicknesses. Previously, it was also shown that a decrease in supersaturation may lead to the rough-to-smooth transition of the crystal growth mechanism^{30–32}. We have experimentally found that during the same deposition process, nanoribbons less than 15 nm thick have a rough surface, while ribbons more than 15 nm thick have a smooth morphology, indicating a 2D growth mechanism. This suggests that a transition from rough to smooth growth takes place in our experiment. Moreover, this growth scenario is consistent with the appearance of a high yield of thin nanoribbons. At some point, the growth particles from the vapour cannot saturate the side edge of very thick seeds, and the chemical potential of the crystal itself becomes larger than that of the vapour $(p_0 > p)$. In this case, the growth of the thickest nanoribbons may stop, while the growth rate of crystals from saturated seeds increases with a decrease in their thickness²⁹. As we will show below, the difference in morphology between thicker and thinner nanoribbons strongly affects the transport properties of the topological surface states.

Transport measurements of Bi_2Se_3 nanoribbons

 ${\bf Bi_2Se_3}$ nanoribbons synthesized using the parameter $t_2=0$ min were transferred to a Si/SiO $_2$ (300 nm) substrate for transport measurements. After the transfer, several nanoribbons were selected using optical and atomic force microscopies. The electrical leads were patterned via electron-beam lithography to create contacts for magnetoresistance and Hall effect measurements. Ar⁺-ion beam etching was used to remove the native oxide from the top surface of the nanoribbons prior to the deposition of Ti/Au contacts (3/80 nm) (Fig. 3).

The longitudinal resistance R_{xx} was measured from room temperature down to 2 K (shown in the insets of Fig. 4a). The metallic behavior is observed for both thin and thick ribbons as well as for previously reported $\mathbf{Bi_2Se_3}$ nanoribbons/nanowires with different thicknesses^{21,33}. This dependence is expected since the $\mathbf{Bi_2Se_3}$ nanostructures grown by the PVD method usually contain native defects such as selenium vacancies, which act as electron donors (n-type doping), thereby shifting the Fermi level into the conduction band^{34,35}. We measured the Hall resistance R_{xy} to estimate the sheet carrier density n_{2D} of individual nanoribbons (Fig. 4a). The latter is given by:

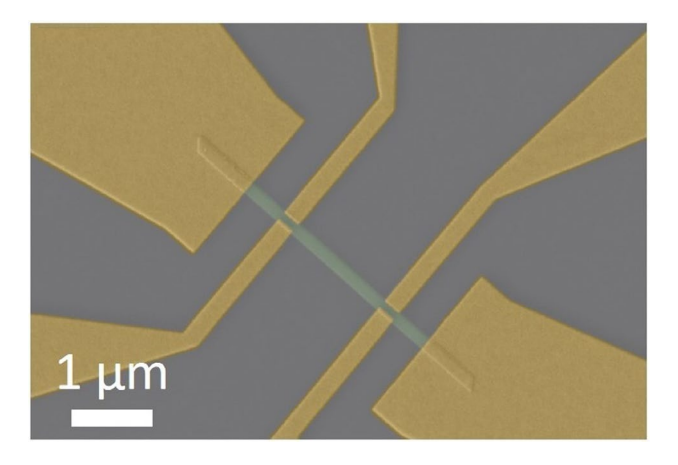


Fig. 3. False-color SEM image of a fabricated device based on a $\mathbf{Bi_2Se_3}$ nanoribbon (green) transferred to a Si/SiO₂ substrate (grey). The metal electrodes are shown in yellow.

$$\frac{1}{n_{2D} \cdot e} = \frac{dR_{xy}}{dB} \times g,\tag{2}$$

where e is the elementary charge, and g is geometrical correction factor. Due to overlapping of the nanoribbon with contact electrodes (the non-ideal Hall bar geometry, see Fig. 3), the measured Hall voltage needs to be corrected 36 . Using a finite element simulation method (COMSOL Multiphysics), we numerically solved the current continuity equation and obtained the correction factor $g\approx 4$ for our Hall bar geometries and contact resistances 19 . The values of n_{2D} extracted from the data are respectively 1.2×10^{13} cm $^{-2}$ for Device~I (thickness t=12 nm, and width w=360 nm), and 8.8×10^{12} cm $^{-2}$ for Device~II (thickness t=22 nm, and width w=310 nm), while the negative slope indicates n-type carriers for both devices. The estimated values of Hall mobility obtained for Device~II and Device~II are $\mu_1=1075$ and $\mu_2=1210$ cm 2 /V·s, respectively.

The magnetoresistance R_{xx} as a function of a magnetic field (up to 12 T) applied perpendicularly to the

The magnetoresistance R_{xx} as a function of a magnetic field (up to 12 T) applied perpendicularly to the surface of the nanoribbons was also measured at low temperatures (2 K). Thin $\mathbf{Bi_2Se_3}$ nanoribbons with thickness below 15 nm show well-pronounced magnetoresistance oscillations in the entire range of the magnetic fields, while for thicker nanoribbons they are only visible at high fields (Fig. 4b). As we will discuss below, this difference can be explained by the coherent scattering of electron waves from surface irregularities associated

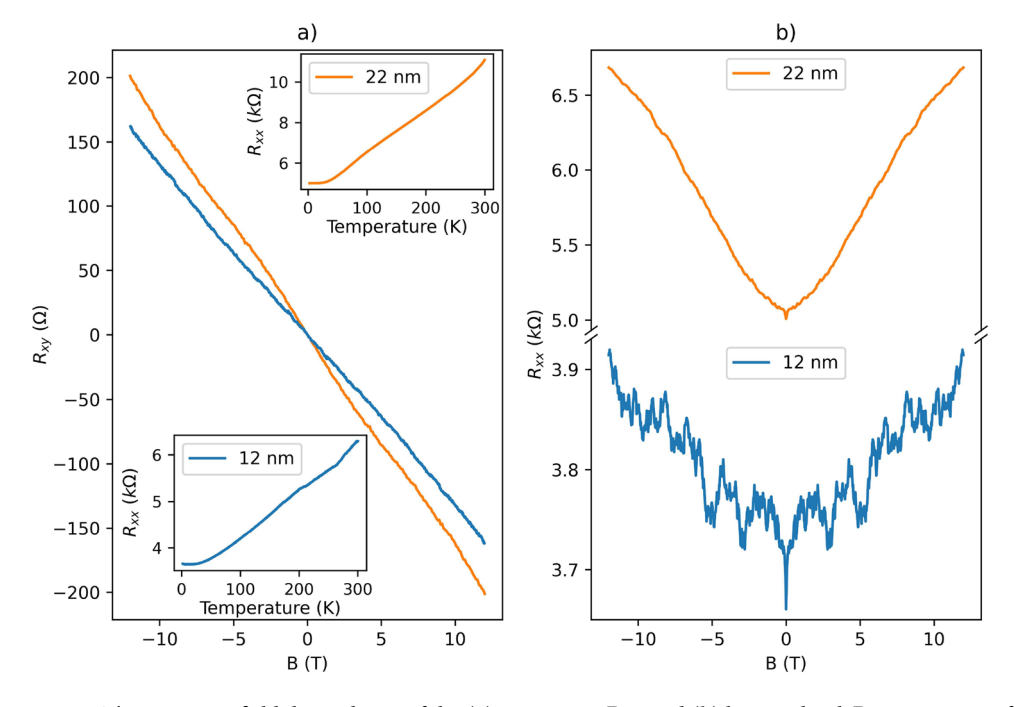


Fig. 4. The magnetic field dependence of the (a) transverse R_{xy} and (b) longitudinal R_{xx} resistances for 12 nm (blue, *Device I*) and 22 nm (orange, *Device II*) thick ribbons measured at 2 K, respectively. The insets in (a) represent the temperature dependence of R_{xx} for the two devices.

with the peculiar morphology of the thin nanoribbons (due to different growth mechanisms compared to the thicker ones), which leads to the appearance of AAS-like orbits.

For the thick nanoribbon (t=22 nm, $Device\ II$), pronounced oscillations were found by subtracting a polynomial background (Supplementary Information 1, Fig. S1) and plotting the data in 1/B (see inset of Fig. 5a). The observed oscillations are associated with a quantum phenomenon known as Shubnikov-de Haas oscillations and can be related to the cross-sectional area of the Fermi surface in momentum-space via the Onsager relation^{33,37}. Fourier transform (FT) analysis (Fig. 5a) on the SdH oscillations was performed to find out the oscillation frequencies. Thus, the frequencies $F_1^{II}=18.7\ \mathrm{T}$ and $F_2^{II}=37.2\ \mathrm{T}$ were identified, corresponding to $n_{2D-1}^{II}=4.52\times10^{11}\ \mathrm{cm}^{-2}$ and $n_{2D-2}^{II}=8.99\times10^{11}\ \mathrm{cm}^{-2}$ according to the Onsager relationship. The presence of two frequency peaks is at the origin of the observed beating pattern of the SdH oscillations³⁸.

We have previously demonstrated a multi-frequency pattern similar to the one reported here for nanoribbons thicker than 30 nm³³. Notably, the corresponding frequencies remained unaffected by applying a high back-gate voltage, indicating that they originate either from the bulk states or from the top Dirac surface states (at the interface of the nanoribbon with vacuum)³³. This interpretation is supported by nearly one order-of-magnitude discrepancy between the 2D carrier densities extracted from Hall effect measurements and those derived from SdH oscillations. As has been shown, a charge accumulation layer with $n_{2DEG} \approx 1.0 \times 10^{13}$ cm⁻² is formed at the nanoribbon-substrate interface and dominates in the Hall conductance^{19,33}. Since the bottom topological surface states (TSSs) overlap with the accumulation layer with much lower mobility, SdH oscillations due to this 2DEG do not usually appear in the magnetoresistance. Considering these findings, we conclude that the observed frequencies in the SdH spectrum originate from either bulk states or surface carriers at the interface with a vacuum, consistent with the behaviour reported in Ref_c^{33} .

As shown in Fig. 4b, thin nanoribbons (less than 15 nm) exhibit instead a strong oscillatory pattern in the entire range of a magnetic field. The phenomenology of these oscillations is compatible with that of universal conductance fluctuations (UCF). The latter represents quantum interferences of electron diffusion paths with different lengths, leading to aperiodic oscillations in magnetic field³⁹. However, the FT calculated from $\Delta R_{xx}(B)$ below 7 T (to exclude the possible impact of SdH on the magnetoresistance) shows instead a dominant peak at $F_{UCF}^I = 0.41 \, \mathrm{T}^{-1}$ (Fig. 5b, *Device I*). A well-defined periodicity is unusual for conventional UCF (Supplementary Information 2, Fig. S2). However, it can be explained if the fluctuations originate from Altshuler-Aronov-Spivak-type orbits, with similar characteristic areas that become accessible because of the specific surface morphology of the thin nanoribbons.

A comparable phenomenology was previously reported in Refs. 40,41, where periodic Aharonov-Bohm (AB) oscillations were observed in the magnetotransport of Bi₂Se₃ films and Bi₂Te₃ flakes. These materials exhibited characteristic pyramidal domains on their surfaces, and the length scale of the observed AB orbits corresponded to the typical perimeter of triangular terraces found on the surface. Tunneling spectroscopy performed in Refs. 42,43 further demonstrated that the local density of states is strongly enhanced near these step edges on Bi₂Se₃ and Bi₂Te₃, confirming that they act as preferential electron trajectories. In our case, the characteristic length scale of the observed oscillations corresponds to the circumference of similarly sized circular grains on the surface of the thin nanoribbons (see Fig. S3, Supplementary Information 3), strongly indicating that the periodic magneto-fingerprint originates from coherent electron wave scattering at their step edges. While AB-type oscillations were dominant in the previous studies, they are unlikely to appear in our system due to the

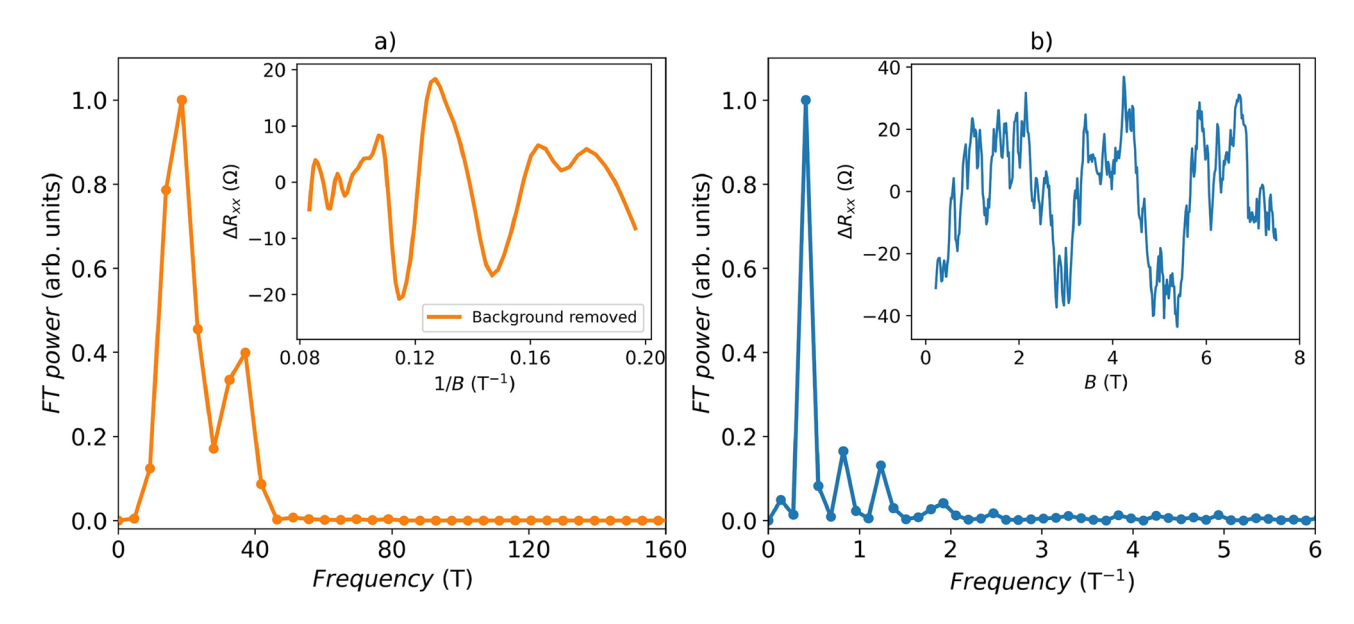


Fig. 5. Power spectra of (a) $\Delta R_{xx}(1/B)$ (shown in the inset) for a 22 nm thick (*Device II*) nanoribbon and (b) $\Delta R_{xx}(B)$ (in the inset) for a 12 nm thick ribbon (*Device II*) measured at 2 K, respectively. A 5^{th} -order polynomial was subtracted to remove the magnetoresistance background.

significantly larger dimensions of the device containing a large number of grains, which would average out such effects. Nonetheless, the presence of uniform circular grains on the nanoribbon surface can support closed-loop paths around their perimeter, enabling AAS-type interference (Supplementary Information 4, Fig. S4). Given the uniformity in grain dimensions, we expect a periodic modulation in conductance as a function of magnetic field, with a characteristic period determined by the enclosed area. Unlike AB oscillations, AAS oscillations are not averaged out in ensembles of rings and should persist, leading to robust interference signatures in the magnetoconductance⁴⁴.

The characteristic AAS area of these orbits can be calculated as $S = \phi \times F_{UCF}^I$, where $\phi = h/2e$ is the magnetic flux quantum relevant for AAS oscillations. From the extracted orbit area $S = 0.0008~\mu\text{m}^2$ one can estimate a characteristic path length for the electrons as $L \sim 2\sqrt{\pi S} = 100$ nm. The calculated value $2R_{AAS} = 32$ nm (for circular orbits $L = 2\pi R_{AAS}$) is in good agreement with the characteristic size of the surface irregularities of about 29.4±1.6 nm, which was extracted using the two-dimensional fast Fourier transform of the AFM image presented in the inset of Fig. 2a (Supplementary Information 3).

Further analysis will be associated with *Device III*, fabricated using a $\mathbf{Bi_2Se_3}$ nanoribbon with a maximized surface-to-volume ratio (thickness t=12 nm, and width w=85 nm). For this device, the $R_{xx}(B)$ pattern changed after warming up to room temperature (Fig. 6a), which excludes that the magnetoresistance oscillations can be only attributed to SdH oscillations (Fig. S5, Supplementary Information 5). Moreover, the onset of SdH oscillations requires the condition $\mu B \gg 1$, where μ is the electron mobility. This condition is not usually satisfied below 5-6 T, since typical Hall mobility values in nanoribbons are between 1200-2100 cm²/V·s as reported in our previous works 19,33. Therefore, we attribute the observed oscillations in the low magnetic field to the coherent AAS-like orbits with a similar characteristic area, analogous to *Device I* and conventional UCF.

To determine whether these oscillations come from interference effects in the bulk or from the 2D topological surface, we have studied the angular dependence of R_{xx} with respect to the out-of-plane magnetic field. In an ideal 2D electron system, the interference pattern depends only on the normal component of the magnetic field $B_{\perp} = B\cos\theta$, where θ is the angle between the direction normal to the nanoribbon plane and the orientation of the magnetic field⁴⁵. After subtracting a 5th-order polynomial background, the resulting oscillation patterns ΔR_{xx} measured at various angles θ superimpose if plotted against $1/B_{\perp}$ below 5 T, which confirms the 2D origin of UCF⁴⁰ (Fig. 6b). However, the analysis becomes more complicated at higher fields due to the coexistence of UCF, AAS and SdH oscillations. The coherence of the AAS-like orbits associated with the specific morphology of the samples is also observable at higher magnetic fields and can overlap with SdH oscillations.

The R_{xx} as a function of the gate voltage has been studied for *Device III*. In addition to the expected increase of the resistance due to the depletion of the nanoribbon carriers by the gate, we also observe reproducible oscillations of R_{xx} as a function of back-gate voltage (Fig. 7a). We now contend that size quantization effects are essential in our devices.

The band structure of surface carriers in TI nanoribbons is described by the momentum vector k along the nanoribbon axis and the angular momentum $l^{46,47}$:

$$E_l(k) = \pm \hbar v_F \sqrt{k^2 + \frac{\pi(l)^2}{S}},$$
 (3)

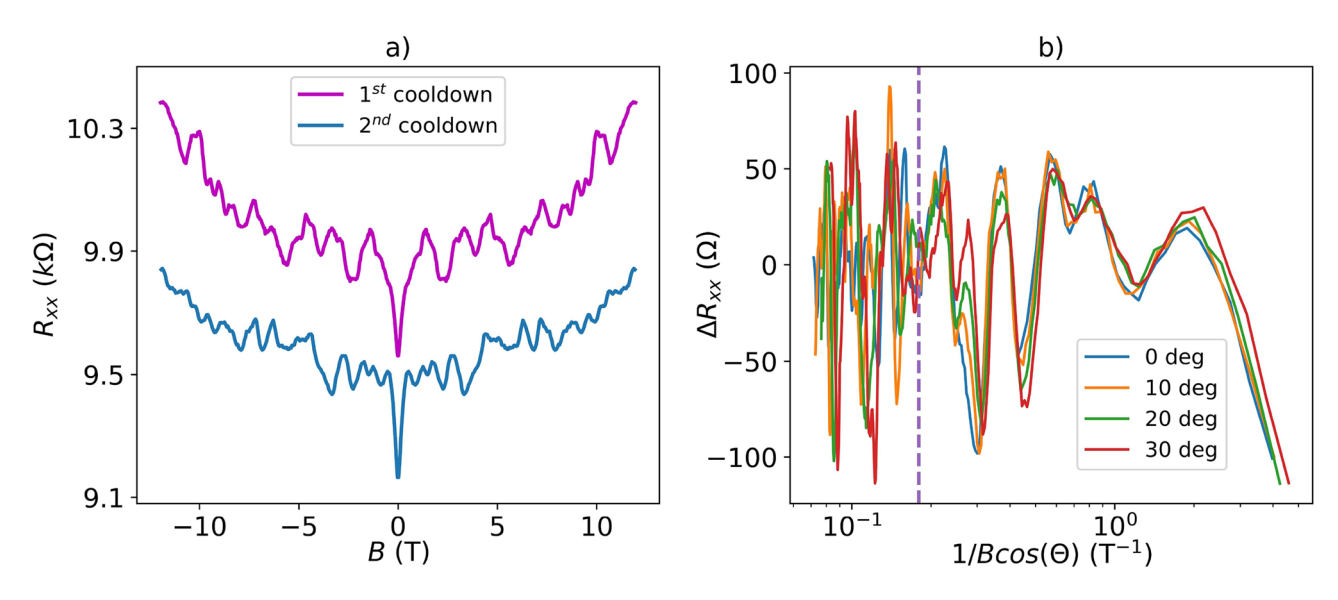
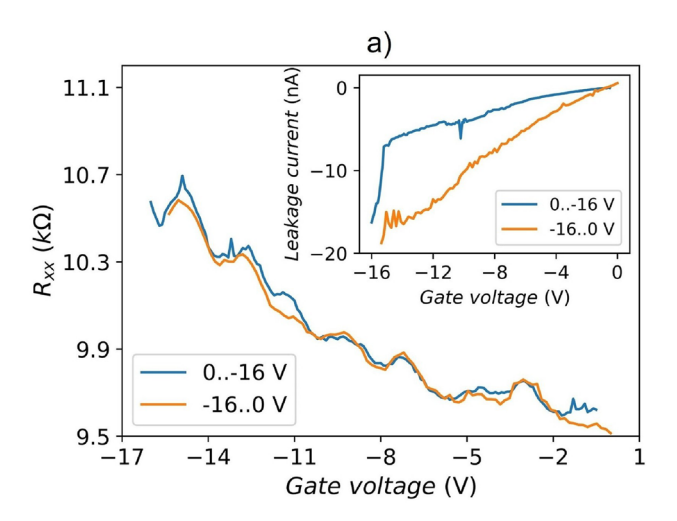


Fig. 6. (a) The magnetoresistance of *Device III* (thickness t=12 nm, and width w=85 nm) as a function of a magnetic field after the first and second cooldowns, measured at 2 K. (b) Background-removed (5^{th} -order polynomial) resistance ΔR_{xx} as a function of $1/B\cos\theta$. The x-axis is plotted on a logarithmic scale to show a clear data superimposition at low magnetic fields. The vertical dashed line denotes a magnetic field of 5.5 T.



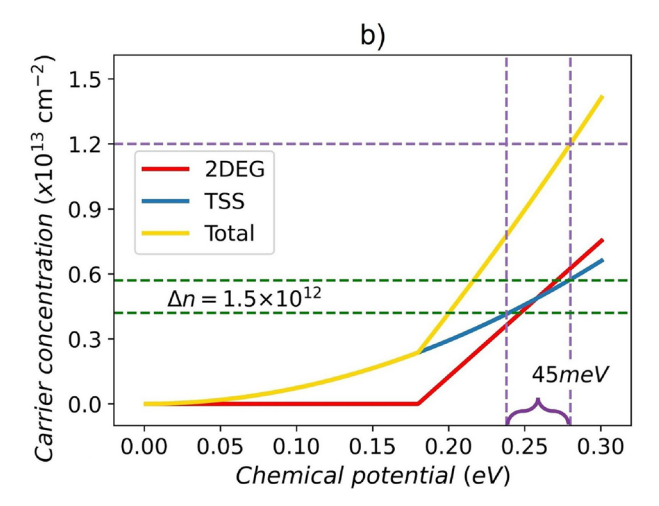


Fig. 7. (a) R_{xx} as a function of back-gate voltage (*Device III*, T=2 K). Blue and orange curves represent two scan sweeps with different directions (see more data in Fig. S6 of Supplementary Information 6). The leakage current was continuously monitored and kept below 3 % of the measured signal (inset). (b) Charge carrier concentration as a function of Fermi energy. The red line shows the dependence for a regular 2DEG, the blue line for Dirac states, and the yellow one for the substrate/nanoribbon interface, where both types of carriers exist.

where l is half-integer $\pm \frac{1}{2}, \pm \frac{3}{2}, ..., \hbar$ is the reduced Planck constant, v_F is Fermi velocity (5 × 10⁵ ms⁻¹), S is the cross-sectional area of the nanoribbon. When the chemical potential crosses one sub-band, a new conduction channel becomes accessible, leading to pronounced resistance dips⁴⁶. We argue that the oscillations observed in $R_{xx}(V_g)$ are directly related to sub-bands formation, as described by Eq. 3. To support this interpretation, we perform the following analysis: first, we calculate the carrier concentration as a function of chemical potential; second, we estimate how the carrier concentration changes with an applied gate voltage (see Fig. 7b). Finally, we compare the change in chemical potential induced by the applied gate voltage with the number of resistance oscillations observed in our measurements.

The charge carrier concentration of a trivial 2DEG is given by $n_{2DEG}=k_F^2/2\pi$. The corresponding Fermi energy can be calculated as:

$$E_{F(2DEG)} = \frac{\hbar^2 k_F^2}{2m^*} = \frac{\hbar^2 \pi}{m^*} n_{2DEG},\tag{4}$$

where k_F is Fermi wavevector, m^* is effective mass, for the $\mathbf{Bi_2Se_3}$ case $m^*=0.15m_e^{-33}$. For Dirac fermions the carrier concentration is $n_{SS}=k_F^2/4\pi$, and the Fermi energy can be written as:

$$E_{F(SS)} = \hbar k_F v_F = \hbar v_F \sqrt{4\pi n_{SS}}.$$
 (5)

Since the gate voltage primarily affects the charge carrier concentration at the substrate/nanoribbon interface 38 , the position of the Fermi level can be estimated from the total carrier concentration at the substrate/nanoribbon interface using Eqs. 4 and 5, considering that the conduction band minimum is located 180 meV above the Dirac point 33 . For a typical carrier concentration in our nanoribbons on a Si/SiO $_2$ substrate of $n=1.2\times10^{13}$ cm $^{-2}$, the calculated E_F is \approx 270 meV. The contributions to the total carrier concentration as a function of the chemical potential measured from the Dirac point are shown in Fig. 7b: the blue line represents the bottom TSSs, the red line is the trivial 2DEG, and the yellow one is the sum of the two.

To estimate the carrier concentration change induced by the applied gate voltage, we have numerically computed the capacitance between the back-gate electrode and the bottom surface of the 3D-TI nanoribbon using COMSOL Multiphysics. So, considering a simple asymmetric metallic parallel plate geometry, where one electrode is given by the doped silicon and the other is the nanoribbon, the static surface charge carrier density per applied gate voltage $\sigma \simeq 1.5 \times 10^{-4}$ C/m²-V was numerically calculated.

Based on this value of σ , the change in carrier concentration at the bottom interface can be estimated using the relation $\Delta n = \sigma V_g/e$. For the maximum applied voltage $(V_g = -16 \text{ V})$, this yields $\Delta n = 1.5 \times 10^{12} \text{ cm}^{-2}$. We can assume that the change of carrier concentration occurs mainly in the bottom TSSs (Supplementary Information 7). This is justified by the fact that the trivial 2DEG at the bottom extends well inside the bulk, and therefore does not feel the electric field of the gate potential that is screened by the TSS³8. In this case, the Δn corresponds to a change in the chemical potential of $\approx 45 \text{ meV}$ (see Fig. 7b). For the dimensions of the nanoribbon in this study (*Device III*), we find that the distance between the sub-band minima $\Delta = hv_F/C \approx 9 \text{ meV}$, where h is the Planck constant and C = 2(w+t) is the circumference of the nanoribbon with rectangular cross-section⁴8,⁴9. The change in the chemical potential would therefore correspond to the crossing of approximately 5 sub-bands which is very close to the 5 to 6 $R_{xx}(V_g)$ oscillations observed in Fig. 7a.

An alternative approach to reveal the quantization effect through sub-band formation is to apply an in-plane magnetic field. In the presence of a magnetic field applied along the TI nanoribbon, Eq. 3 can be rewritten as:

$$E_l(k) = \pm \hbar v_F \sqrt{k^2 + \frac{\pi (l - \phi/\phi_0)^2}{S}},$$
(6)

where $\phi = BS$ is a magnetic flux threading the cross-section area S of the nanoribbon, and, $\phi_0 = h/e$ is the fundamental flux quantum. According to Eq. 6, the energy-momentum relation is periodic in ϕ/ϕ_0 , which leads to the appearance of AB oscillations of G_{xx}^{47} (Fig. 8a).

In the quasi-ballistic regime, h/e AB oscillations are predicted to dominate over h/2e AAS oscillations 47 . AAS oscillations originate from interference between time-reversed paths, due to weak anti-localization and, thus, differ from AB oscillations in their physical origin. In this regime, the circumference of the nanoribbon should not be much longer than the mean-free path l_e . The pattern of these oscillations also depends on the carrier density, which can be changed by applying a gate voltage. At the Dirac point, magnetoconductance minimum at $\phi/\phi_0=0$ and maximum at $\phi/\phi_0=0.5$ should be observed. However, even away from the Dirac point, the AB phase can alternate with applied gate voltage, when E_F is crossing the sub-bands Fig. 8 presents the magnetoconductance as a function of two different back-gate voltages (0 and -8 V), demonstrating that maxima and minima at finite magnetic flux alternate with an applied gate and the period oscillation at $V_g=0$ V is close to ϕ_0 as shown by the Fourier transform of $\partial G_{xx}/\partial(\phi/\phi_0)$.

However, there is also a component in the FT at approximately twice the frequency that can be attributed to AAS. This can be explained by the presence of a strong weak anti-localization peak (Fig. 6a), which indicates that a fraction of modes has a more diffusive character. Since the gate voltage was not high enough to tune the chemical potential to the Dirac point, the alternating maxima and minima of G_{xx} as a function of gate voltage indicate the crossing of sub-bands by the Fermi level. This behavior has not previously been observed in non-topological systems⁴⁷. The fact that by decreasing the gate voltage the ratio between the AB and AAS inverts (Fig. 8b) might be due to more diffusive modes contributing at $V_q = -8$ V.

Conclusions

In summary, we have demonstrated the reproducible and controllable growth of large quantities of ultrathin 3D-TI ${\bf Bi_2Se_3}$ nanoribbons via physical vapour deposition, along with their systematic transport characterisation. The resulting nanoribbons exhibit Hall mobility in the range of 1000–2000 cm²/V·s, often up to an order of magnitude higher than in many ternary or quaternary topological insulator compounds, such as $({\rm Bi_1}_{-x}{\rm Sb_x})_2{\rm Te_3}$ or ${\rm Bi_2}_{-x}{\rm Sb_x}{\rm Te_3}_{-y}{\rm Se_y}^{17,50-53}$.

We show that the nanoribbon growth kinetics can be tuned from a 2D layer-by-layer to a rough mode by adjusting synthesis parameters. A strong correlation between nanoribbon morphology and transport properties is demonstrated. The oscillatory pattern of magnetoresistance observed over the entire range of the

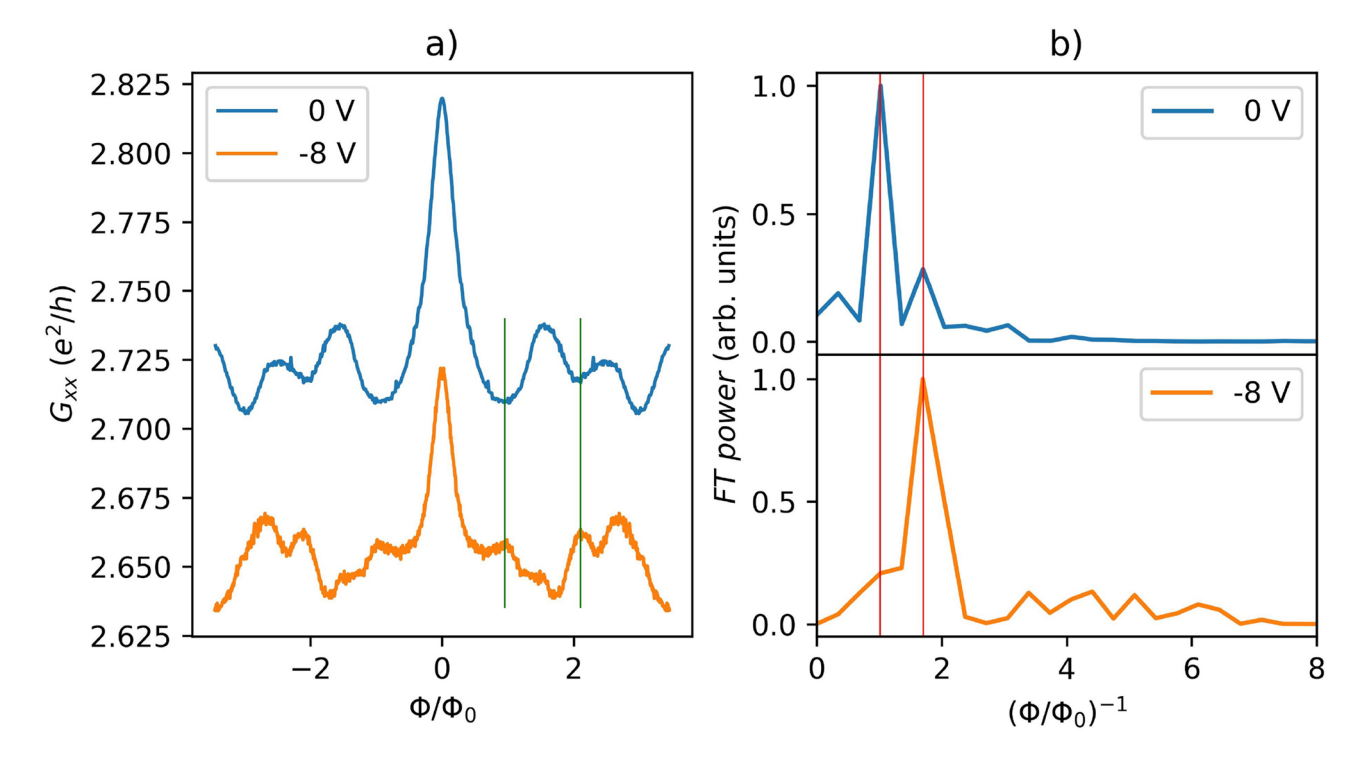


Fig. 8. (a) The magnetoconductance as a function of ϕ/ϕ_0 for two different back-gate voltages 0 and -8 V (*Device III*). The measurements were carried out at a temperature of 2 K. (b) Fourier transforms of $\partial G_{xx}/\partial (\phi/\phi_0)$ from panel (a).

magnetic field for ultrathin nanoribbons is explained by coherent Altshuler-Aronov-Spivak-like orbits with similar characteristic areas, which become accessible due to the specific surface morphology. Additionally, the superposition effect between AAS and SdH oscillations is observed at high magnetic fields.

While the main achievement of this study is the demonstration of a scalable and cost-effective route to ultrathin nanoribbons, we have *occasionally* obtained several ultranarrow nanoribbons with widths below 100 nm and thicknesses under 15 nm. In these exceptional cases, the nanoribbon circumference becomes smaller than the dephasing length, making sub-band quantization effects (manifesting as an oscillatory behaviour of the magnetoresistance as a function of back-gate voltage) significant in transport measurements.

The proposed growth method allows effective control over thickness via deposition time; however, the width of the nanoribbons remains dependent on the lateral dimensions of the seed plates. One potential approach to overcome this limitation is combining the time-controlled growth parameters demonstrated in this study with a Vapor-Liquid-Solid (VLS) approach, using catalyst particles to define ribbon width. This hybrid strategy could enable systematic growth of ultranarrow and ultrathin nanoribbons. It can be developed based on our previous experience with VLS growth of ${\bf Bi_2Se_3}$ (used for high-yield growth of thicker nanoribbons⁵⁴), and provides a promising route to achieving surface-state-dominated transport in highly confined topological insulator nanostructures.

Data availability

Data sets generated during the current study are available from the corresponding author on reasonable request.

Received: 11 June 2025; Accepted: 8 October 2025

Published online: 31 October 2025

References

- 1. Manousakis, J., Altland, A., Bagrets, D., Egger, R. & Ando, Y. Majorana qubits in a topological insulator nanoribbon architecture. *Phys. Rev. B* https://doi.org/10.1103/PhysRevB.95.165424 (2017).
- Sarma, S. D., Freedman, M. & Nayak, C. Majorana zero modes and topological quantum computation. npj Quantum Inf. https://doi.org/10.1038/npjqi.2015.1 (2015).
- Sun, X. et al. Realization of superconducting transmon qubits based on topological insulator nanowires. Appl. Physi. Lett. https://doi.org/10.1063/5.0140079 (2023).
- Schmitt, T. W. et al. Integration of topological insulator Josephson junctions in superconducting qubit circuits. Nano Lett. https://doi.org/10.1021/acs.nanolett.1c04055 (2022).
- Hwang, T.H., Kim, H.S., Kim, H., Kim, J.S. & Doh, Y.J. Electrical detection of spin-polarized current in topological insulator Bi_{1.5} Sb_{0.5}Te_{1.7}Se_{1.3}. Current Applied Physics (2019) https://doi.org/10.1016/j.cap.2019.04.015.
- Yang, F. et al. Switching of charge-current-induced spin polarization in the topological insulator BiSbTeSe₂. Phys. Rev. B https://doi.org/10.1103/PhysRevB.94.075304 (2016).
- Acosta, C. M. & Fazzio, A. Spin-polarization control driven by a rashba-type effect breaking the mirror symmetry in twodimensional dual topological insulators. *Phys. Rev. Lett.* https://doi.org/10.1103/PhysRevLett.122.036401 (2019).
- Park, H. et al. Enhanced spin-to-charge conversion efficiency in ultrathin Bi₂Se₃ observed by spintronic terahertz spectroscopy. ACS Appl. Mater. Interfaces https://doi.org/10.1021/acsami.1c03168 (2021).
- 9. Wang, T. H. & Jeng, H. T. Topological insulator nanoribbons a new paradigm for high thermoelectric performance. *Nano Energy* https://doi.org/10.1016/j.nanoen.2019.104092 (2019).
- Xiong, Y. et al. Chemically switchable n-type and p-type conduction in bismuth selenide nanoribbons for thermoelectric energy harvesting. ACS Nano https://doi.org/10.1021/acsnano.0c08685 (2021).
- 11. Yang, N. X., Yan, Q. & Sun, Q. F. Linear and nonlinear thermoelectric transport in a magnetic topological insulator nanoribbon with a domain wall. *Phys. Rev. B* https://doi.org/10.1103/PhysRevB.102.245412 (2020).
- 12. Ye, X., Xu, H. & Zhu, X. Spin thermoelectric effects of skyrmions in ferromagnetic topological insulators. *J. Phys. D: Appl. Phys.* https://doi.org/10.1088/1361-6463/acaed9 (2023).
- Saxena, R. et al. Electronic confinement of surface states in a topological insulator nanowire. *Phys. Rev. B* https://doi.org/10.1103/ PhysRevB.106.035407 (2022).
- Arakane, T. et al. Tunable dirac cone in the topological insulator Bi_{2-x}Sb_xTe_{3-y}Se_y. Nat. Commun. https://doi.org/10.1038/ncomms1639 (2012).
- 15. Jafarpisheh, S. et al. Reducing the impact of bulk doping on transport properties of Bi-based 3D topological insulators. *Phys. Status Solidi* (b) https://doi.org/10.1002/pssb.202000021 (2021).
- 16. Ren, Z., Taskin, A. A., Šasaki, S., Šegawa, K. & Ando, Y. Optimizing Bi_{2-x}Sb_xTe_{3-y}Se_y solid solutions to approach the intrinsic topological insulator regime. *Phys. Rev. B* https://doi.org/10.1103/PhysRevB.84.165311 (2011).
- 17. Hong, S. S., Cha, J. J., Kong, D. & Cui, Y. Ultra-low carrier concentration and surface-dominant transport in antimony-doped $\mathrm{Bi}_2\mathrm{Se}_3$ topological insulator nanoribbons. *Nat. Commun.* https://doi.org/10.1038/ncomms1771 (2012).
- Nowak, K. et al. Influence of doping on the topological surface states of crystalline Bi₂Se₃ topological insulators. Materials htt ps://doi.org/10.3390/ma15062083 (2022).
- 19. Kunakova, G. et al. High-mobility ambipolar magnetotransport in topological insulator Bi_2Se_3 nanoribbons. Phys. Rev. Appl. h ttps://doi.org/10.1103/PhysRevApplied.16.024038 (2021).
- Wiesner, M. et al. The effect of substrate and surface plasmons on symmetry breaking at the substrate interface of the topological insulator Bi₂Te₃. Sci. Rep. https://doi.org/10.1038/s41598-019-42598-9 (2019).
- Andzane, J. et al. Catalyst-free vapour–solid technique for deposition of Bi₂Te₃ and Bi₂Se₃ nanowires/nanobelts with topological insulator properties. Nanoscale https://doi.org/10.1039/C5NR04574F (2015).
- Kong, D. et al. Few-layer nanoplates of Bi₂Se₃ and Bi₂Te₃ with highly tunable chemical potential. Nano Lett. https://doi. org/10.1021/nl101260j (2010).
- 23. Rockett, A. Physical vapor deposition. Mater. Sci. Semicond. https://doi.org/10.1007/978-0-387-68650-9_11 (2008).
- 24. Lovette, M. A. et al. Crystal shape engineering. Ind. Eng. Chem. Res. https://doi.org/10.1021/ie800900f (2008).
- Dai, Z. R., Pan, Z. W. & Wang, Z. L. Novel nanostructures of functional oxides synthesized by thermal evaporation. Adv. Funct. Mater. https://doi.org/10.1002/adfm.200390013 (2003).
- 26. Li, Y., Liu, Y., Lee, C. S. & Lee, S. T. Large-scale synthesis of Ga_2O_3 nanoribbons by a two-step gas flow control. Superlattices Microstruct. https://doi.org/10.1016/j.spmi.2009.05.006 (2009).
- 27. Yan, C., Singh, N. & Lee, P. S. Morphology control of indium germanate nanowires, nanoribbons, and hierarchical nanostructures. *Cryst. Growth Des.* https://doi.org/10.1021/cg900406d (2009).

- Wang, Z. L. Nanobelts, nanowires, and nanodiskettes of semiconducting oxides from materials to nanodevices. Adv. Mater. https://doi.org/10.1002/adma.200390100 (2003).
- 29. Nebol'sin, V., Levchenko, E., Yuryev, V. & Swaikat, N.,. About the Shape of the Crystallization Front of the Semiconductor Nanowires. ACS Omega https://doi.org/10.1021/acsomega.2c06475 (2023).
- 30. Elwenspoek, M. & Boerhof, W. Anisotropic growth rate of rough crystal faces. *Phys. Rev. B* https://doi.org/10.1103/PhysRevB.36.5326 (1987).
- 31. Liu, X. Y., Bennema, P. & Eerden, J. P. V. D. Rough–flat–rough transition of crystal surfaces. *Nature* https://doi.org/10.1038/356778a0 (1992).
- 32. Tilbury, C. J. & Doherty, M. F. Modeling layered crystal growth at increasing supersaturation by connecting growth regimes. AIChE J. https://doi.org/10.1002/aic.15617 (2017).
- Kunakova, G. et al. Bulk-free topological insulator Bi₂Se₃ nanoribbons with magnetotransport signatures of dirac surface states. Nanoscale https://doi.org/10.1039/C8NR05500A (2018).
- Sapkota, Y.R. Development of Novel Electronic and Magnetic Thin Films for Next Generation Spintronics Applications. Ph.D. thesis, Southern Illinois University at Carbondale. https://opensiuc.lib.siu.edu/dissertations/2027 (2022).
- 35. Devidas, T. R. et al. Role of Se vacancies on Shubnikov-de Haas oscillations in Bi₂Se₃: A combined magneto-resistance and positron annihilation study. *Europhys. Lett.* https://doi.org/10.1209/0295-5075/108/67008 (2015).
- 36. Barbut, L., Jazaeri, F., Bouvet, D. & Sallese, J. M. Mobility measurement in nanowires based on magnetic field-induced current splitting method in H-shape devices. *IEEE Trans. Electron Devices* https://doi.org/10.1109/TED.2014.2321284 (2014).
- 37. Shoenberg, D. Magnetic oscillations in metals. https://doi.org/10.1017/CBO9780511897870 (2009).
- 38. Veyrat, L. et al. Band bending inversion in Bi₂Se₃ nanostructures. Nano Lett. https://doi.org/10.1021/acs.nanolett.5b03124 (2015).
- 39. Pan, H. et al. Nontrivial surface state transport in Bi_2Se_3 topological insulator nanoribbons. Appl. Phys. Lett. https://doi.org/10.1063/1.4975386 (2017).
- 40. Kandala, A., Richardella, A., Zhang, D., Flanagan, T. C. & Samarth, N. Surface-sensitive two-dimensional magneto-fingerprint in mesoscopic Bi_2Se_3 channels. Nano Lett. https://doi.org/10.1021/nl4012358 (2013).
- Charpentier, S. et al. Induced unconventional superconductivity on the surface states of Bi₂Te₃ topological insulator. *Nat. Commun.* https://doi.org/10.1038/s41467-017-02069-z (2017).
- Liu, Y., Weinert, M. & Li, L. Spiral growth without dislocations: Molecular beam epitaxy of the topological insulator Bi₂Se₃ on epitaxial graphene/SiC(0001). *Phys. Rev. Lett.* https://doi.org/10.1103/PhysRevLett.108.115501 (2012).
- Alpichshev, Z., Analytis, J. G., Chu, J.-H., Fisher, İ. R. & Kapitulnik, A. STM imaging of a bound state along a step on the surface of the topological insulator Bi, Te₃. Phys. Rev. B https://doi.org/10.1103/PhysRevB.84.041104 (2011).
- Umbach, C. P., Van Haesendonck, C., Laibowitz, R. B., Washburn, S. & Webb, R. A. Direct observation of ensemble averaging of the Aharonov-Bohm effect in normal-metal loops. *Phys. Rev. Lett.* https://doi.org/10.1103/PhysRevLett.56.386 (1986).
- 45. Li, Z. et al. Two-dimensional universal conductance fluctuations and the electron-phonon interaction of surface states in Bi₂Te₂Se microflakes. *Sci. Rep.* https://doi.org/10.1038/srep00595 (2012).
- 46. Münning, F. et al. Quantum confinement of the dirac surface states in topological-insulator nanowires. *Nat. Commun.* https://doi.
- org/10.1038/s41467-021-21230-3 (2021).

 47. Cho, S. et al. Aharonov-Bohm oscillations in a quasi-ballistic three-dimensional topological insulator nanowire. *Nat. Commun.* https://doi.org/10.1038/ncomms8634 (2015).
- 48. Jauregui, L. A., Pettes, M. T., Rokhinson, L. P., Shi, L. & Chen, Y. P. Magnetic field-induced helical mode and topological transitions in a topological insulator papaging. *Nat. Nanotechnol.* https://doi.org/10.1032/papag.2015.203 (2016)
- in a topological insulator nanoribbon. *Nat. Nanotechnol.* https://doi.org/10.1038/nnano.2015.293 (2016).
 49. Ziegler, J. et al. Probing spin helical surface states in topological HgTe nanowires. *Phys. Rev. B* https://doi.org/10.1103/PhysRevB.9
- Rößler, M. et al. Top-down fabrication of bulk-insulating topological insulator nanowires for quantum devices. Nano Lett. https://doi.org/10.1021/acs.nanolett.3c00169 (2023).
- 51. Mi, J.-L. et al. Phase separation and bulk p-n transition in single crystals of Bi₂Te₂Se topological insulator. *Adv. Mater.* https://doi.org/10.1002/adma.201203542 (2013).
- Jia, S. et al. Low-carrier-concentration crystals of the topological insulator Bi₂Te₂Se. Phys. Rev. B https://doi.org/10.1103/ PhysRevB.84.235206 (2011).
- 53. Lee, J., Park, J., Lee, J.-H., Kim, J. S. & Lee, H.-J. Gate-tuned differentiation of surface-conducting states in Bi_{1.5}Sb_{0.5}Te_{1.7}Se_{1.3} topological-insulator thin crystals. *Physical Review B* 86, (2012) https://doi.org/10.1103/PhysRevB.86.245321.
- Sondors, R. et al. High-yield growth and tunable morphology of Bi₂Se₃ nanoribbons synthesized on thermally Dewetted Au. Nanomaterials https://doi.org/10.3390/nano11082020 (2021).

Acknowledgements

This work is supported by the European Union's Horizon 2020 Research and Innovation Program (Grant Agreement No. 766714/HiTIMe). Authors would like to thank "Vinnova competence center at the Chalmers University of Technology 2D-TECH" and the Latvian Council of Science (project No. lzp/2019/1/0349). K. Niherysh acknowledges the financial support of the "Strengthening of the capacity of doctoral studies at the University of Latvia within the framework of the new doctoral model", identification no. 8.2.2.0/20/I/006. We also acknowledge support from the Swedish infrastructure for micro- and nanofabrication – MyFab.

Author contributions

K.N.: Investigation, Formal analysis, Data Curation, Methodology, Writing—Original Draft, Visualization; X.P.: Formal analysis, Investigation; A.P.S.: Investigation; A.K.: Investigation, Validation, Writing - Review and Editing; R.S.: Investigation, Resources; J.A.: Resources, Validation; D.E.: Methodology, Resources, Supervision; T.B.: Conceptualization, Methodology, Validation, Formal analysis, Visualization, Writing—Review and Editing, Supervision; F.L.: Conceptualization, Methodology, Validation, Writing—Review and Editing, Supervision, Project administration.

Funding

Open access funding provided by Chalmers University of Technology.

Declarations

Competing interests

The authors declare no competing interests.

Additional information

Supplementary Information The online version contains supplementary material available at https://doi.org/1 0.1038/s41598-025-23622-7.

Correspondence and requests for materials should be addressed to K.N. or F.L.

Reprints and permissions information is available at www.nature.com/reprints.

Publisher's note Springer Nature remains neutral with regard to jurisdictional claims in published maps and institutional affiliations.

Open Access This article is licensed under a Creative Commons Attribution 4.0 International License, which permits use, sharing, adaptation, distribution and reproduction in any medium or format, as long as you give appropriate credit to the original author(s) and the source, provide a link to the Creative Commons licence, and indicate if changes were made. The images or other third party material in this article are included in the article's Creative Commons licence, unless indicated otherwise in a credit line to the material. If material is not included in the article's Creative Commons licence and your intended use is not permitted by statutory regulation or exceeds the permitted use, you will need to obtain permission directly from the copyright holder. To view a copy of this licence, visit https://creativecommons.org/licenses/by/4.0/.

© The Author(s) 2025